A Mixed Radiometric Normalization Method for Mosaicking of High-Resolution Satellite Imagery

Yongjun Zhang, Lei Yu, Mingwei Sun, and Xinyu Zhu

***Abstract*— A new mixed radiometric normalization (MRN) method is introduced in this paper which aims to eliminate the radiometric difference in image mosaicking. The radiometric normalization methods can be classified as the absolute and relative approaches in traditional solutions. Though the absolute methods could get the precise surface reflectance values of the images, rigorous conditions required for them are usually difficult to obtain, which makes the absolute methods impractical in many cases. The relative methods, which are simple and practicable, are more widely applied. However, the standard for designating the reference image needed for these methods is not unified. Moreover, the color error propagation and the two-body problems are common obstacles for the relative methods. The proposed MRN approach combines absolute and relative radiometric normalization methods, by which the advantages of both can be fully used and the limitations can be effectively avoided. First, suitable image after absolute radiometric calibration is selected as the reference image. Then, the invariant feature probability between the pixels of the target image and that of the reference image is obtained. Afterward, an adaptive local approach is adopted to obtain a suitable linear regression model for each block. Finally, a bilinear interpolation method is employed to obtain the radiometric calibration parameters for each pixel. Moreover, the CIELAB color space is adopted to evaluate the results quantitatively. Experimental results of ZY-3, GF-1, and GF-2 data indicate that the proposed method can eliminate the radiometric differences between images from the same or even different sensors.**

***Index Terms*— Adaptive local approach, high-resolution satellite imagery, image mosaicking, mixed radiometric normalization (MRN), multisources imagery, radiometric difference.**

I. Introduction

IN THE application of earth observation, high-resolution satellite imagery (relative to medium-resolution imagery with 10–100 m resolution [1]) as well as its wide-range analysis have become increasingly important [2]–[4]. Due to the limitations of sensor design, the coverage of a single image is limited. To obtain images with large coverage, image mosaicking is usually adopted using images obtained at a different time and even from different sensors. Due to several factors, such as solar incident angle, atmosphere, and illumination condition [5], [6], radiometric difference exists between different images, thereby posing a large problem for image processing and analysis [3], [5]–[7]. In order to eliminate the differences between images, radiometric calibration is necessary, which can be categorized as absolute radiometric calibration and relative radiometric normalization [6], [8]–[11].

Absolute radiometric calibration aims to convert the digital number (DN) value to the surface reflectance using an atmosphere correction model, a radiometric calibration coefficient, and other related atmospheric correction parameters [12]. Studies have shown that absolute radiometric calibration has the ability to convert the DN values of satellite images to surface reflectance precisely [13]. However, most absolute radiometric calibration methods require the properties of atmosphere at the image acquisition time, which are usually difficult to obtain [14]. Therefore, it is impractical to conduct absolute radiometric calibration in many cases [7], [14]–[17].

Relative radiometric normalization adjusts the radiometric information of the target image to that of the reference image [7], [10], [18], [19]. There exist numerous related approaches, most of which aim for change detection. However, relative radiometric normalization with the intent of image mosaicking only is discussed in this paper, which can be divided into nonlinear correction and linear correction. The linear correction methods are more widely used [5]–[7], [10], [14]. Most linear correction approaches based on the hypothesis that the pseudoinvariant features in the target image are linearly related to the corresponding ones at the same location in the reference image [20], [21]. For these approaches, precise invariant feature extraction is the research hotspot, including the manual selection method, principal component analysis (PCA) method [10], multivariate alteration detection (MAD) method [14], iteratively reweighted MAD (IR-MAD) method [22], and iterative slow feature analysis (I-SFA) method [18].

The absolute and relative radiometric normalization approaches are two common solutions between which the latter is more widely applied because the former requires rigorous conditions. Despite the advantage of simplicity and practicability, relative radiometric normalization methods have disadvantages as well. First, the standard for determining the reference image is not unified. As illustrated in [22] and [23], the reference image was considered to be the clearest target image, while in [4], it was in the middle with the minimum distance to the other images. Therefore, for the same group of test data, the reference images selected by different criteria

Manuscript received April 24, 2016; revised November 9, 2016 and January 19, 2017; accepted January 20, 2017. This work was supported in part by the National Natural Science Foundation of China under Grant 41571434, Grant 41322010, and Grant 41301519, and in part by the National Basic Research Program of China under Grant 2012CB719904. *(Corresponding author: Yongjun Zhang.)*

The authors are with the School of Remote Sensing and Information Engineering, Wuhan University, Wuhan 430079, China (e-mail: zhangyj@whu.edu.cn; leiy@whu.edu.cn; mingweis@whu.edu.cn; zhuxinyu@whu.edu.cn).

Color versions of one or more of the figures in this paper are available online at http://ieeexplore.ieee.org.

Digital Object Identifier 10.1109/TGRS.2017.2657582

may vary, thus yielding different calibration results. Also, in conditions where great changes occurred to most of the objects in the overlapped area, or the overlapped area was too small, it may be difficult to obtain the regression calibration parameters. In addition, the two-body problem [4], which means only one image is processed at a time and the calibration relationship between the images is not independent, is a common problem for relative radiometric calibration with the aim of image mosaicking. Although solutions have been proposed [4], they are rather complicated.

According to the above-mentioned analysis, it can be inferred that both absolute and relative radiometric calibration methods have their advantages and limitations. Therefore, it is imperative to combine the advantages and avoid the limitations. In [24], the aerial hyperspectral images after atmospheric correction by fast line-of-sight atmospheric analysis of spectral hypercubes (FLAASH) were considered as the reference images. HJ-1A/B images were calibrated with the reflectivity products of Landsat TM, and the linear transformation relationship between the DN value of the image and the surface reflectance under certain conditions was obtained in [25]. The reflectivity products of SPOT VGT were used as reference images to calibrate Landsat ETM+ images in [2], which yielded results similar to the results produced by the relative radiometric calibration approach based on invariant features in the overlapped area. In [1], the surface reflectivity products of MODIS were selected as reference images to calibrate medium-resolution images, such as Landsat, Advanced Wide Field Sensor, and ASTER, whereby the DN values of the images were transformed into a surface reflectance similar to MODIS. The above-mentioned methods adopt middle or low-resolution images as test data, the majority of which are usually applied in bitemporal image analysis and change detection, thus leading to insufficient research in mosaicking-aimed radiometric calibration of high-resolution images.

The proposed novel solution, which combines both the absolute and relative radiometric normalization approaches, is defined as mixed radiometric normalization (MRN) in this paper. Considering the characteristics in high-resolution images, corresponding improvements are made to enhance the performance effectively. The proposed method contains four steps. First, the suitable image meeting certain criteria is selected as the candidate reference image. Then, the candidate reference image after absolute radiometric calibration is chosen as the reference image. Next, the invariant feature probability of pixels in both target and reference image is extracted by the linear invariant IR-MAD method. Afterward, the target and reference images are separated into tiles by certain rules, which then enable building a relative normalization regression model block by block. Finally, the radiometric correction parameters of each pixel are obtained by bilinear interpolation, from which the calibrated images can be generated. In the proposed method, the surface reflectance products after the absolute radiometric correction are selected as the reference to avoid the problem of choosing suitable reference image in traditional relative normalization methods. Moreover, the reference data selected in the proposed method have the same geographic coverage with the target images. Therefore, the target images can be corrected independently and simultaneously, thus avoiding the color error propagation, and the two-body problems in traditional relative normalization methods. In addition, the selection of the surface reflectance products as the reference could also reduce the influences caused by the atmosphere and other factors in the target images, i.e., the target images, which do not meet the criteria of absolute normalization, can also be corrected to get the analogous effect of the absolute normalization methods, which extends the range of application of the absolute normalization methods to a certain degree. In general, the proposed MRN approach makes full use of the advantages of both absolute and relative radiometric normalization methods. Meanwhile, the limitations of absolute and relative radiometric normalization methods are effectively avoided in the proposed approach. Experimental results indicate that the proposed approach is able to provide an effective solution for the radiometric normalization of high-resolution images in image mosaicking applications.

II. Background Knowledge

As mentioned earlier, absolute and relative radiometric normalization are two common calibration solutions. Some existing methods of them are employed in this paper.

A. FLAASH

There are two general procedures in absolute radiometric calibration: 1) the DN value of the original image is first transformed into irradiance and then to the atmospheric top reflectance by radiometric calibration and 2) atmospheric correction is adopted to convert atmospheric top reflectance to surface reflectance [15]. The principle of absolute radiometric calibration will not be discussed further in this paper since algorithms, such as QUAC, FLAASH, and ATCOR2/3, are mature [25], [26], [27], among which the FLAASH approach is adopted in our experiments. FLAASH is a physics-based correction method built on MODTRAN4 atmospheric correction software developed by the Air Force Phillips Laboratory, Hanscom AFB, and Spectral Sciences Inc [27]. The main goals of this software are to provide: 1) accurate, physics-based derivation of surface and atmospheric properties; 2) minimal computation time requirements; and 3) an interactive, user-friendly interface for running arbitrary MODTRAN calculations [25], [27], [28].

B. *IR*-MAD

MAD was first applied in change detection, where invariant features of sequential images were extracted and used in radiometric calibration in [15]. The IR-MAD approach, the improvement of MAD, was proposed in [22]. IR-MAD is able to automatically extract invariant features from adjacent images with a different acquisition time, which is applicable in recognizing significant changes, especially when the invariant pixel has a small range. The basic principle of MAD is as follows.

Assuming that two images of N-bands with a different acquisition time cover the same area, and then, the pixels

representing the same geographical location can be expressed as $T1 = (T1_1 \dots T1_i \dots T1_N)^T$ and $T2 = (T2_1 \dots T2_i \dots T2_N)^T$, where $T1_i$ and $T2_i$ represent the gray value of the first and second image in band i, respectively. Random variables U and V can be obtained by any linear transformation, such as $a^T = (a_1 \dots a_i \dots a_N)$ and $b^T = (b_1 \dots b_i \dots b_N)$

$$U = a^T T1 = a_1 T1_1 + \dots + a_i T1_i + \dots + a_N T1_N \quad (1)$$

$$V = b^T T2 = b_1 T2_1 + \dots + b_i T2_i + \dots + b_N T2_N. \quad (2)$$

The linear transformation parameters that generate the maximum correlation coefficient between U and V can be obtained by canonical correlation analysis [29]. The MAD variable is the difference between U and V

$$\mathrm{MAD}_i = U_{N-i+1} - V_{N-i+1}, \quad i = 1 \dots N. \quad (3)$$

The sum of the squares of the standardized MAD can be obtained by

$$Z = \sum_{i=1}^{N} \left(\frac{\mathrm{MAD}_i}{\sigma_{\mathrm{MAD}_i}} \right)^2 \quad (4)$$

$$\sigma_{\mathrm{MAD}_i} = \sqrt{\mathrm{Var}(MAD_i)} = \sqrt{2(1 - \rho_{N-i+1})} \quad (5)$$

where σ_{MAD_i} is the standard deviation of the MAD_i, $\mathrm{Var}(\mathrm{MAD}_i)$ is the variance of the MAD_i, and ρ_{N-i+1} is the corresponding canonical variable.

Since the value of Z meets with N degrees of freedom of chi-square distribution, the probability of Z as an invariant point can be described as

$$P(\text{no-change}) = P\{\chi^2(N) > Z\}. \quad (6)$$

IR-MAD is the iterative result of MAD. In the process of the first iteration, the weight of all the pixels is initialized to 1, and the invariant feature probability of each pixel is obtained. During the next iteration, the invariant feature probability of each pixel is considered as its weight and is calculated again by MAD. The iteration continues until it reaches the stopping condition, where the mobility scale of the canonical variable is below a certain threshold, or the iteration time reaches a certain value. After iteration, the invariable pixels have a high weight, while the variable ones do not. The pixels whose invariant feature probability is greater than a certain threshold are selected as the invariant pixels for radiometric normalization purposes.

III. Methods

A. Overview of the Proposed MRN Method

The overall process of the proposed MRN approach, as shown in Fig. 1, can be described as follows.

1) Selection of candidate reference image. The factors of geographical coverage, acquisition time, and spatial resolution were considered to select the suitable image as the candidate reference image.
2) Absolute radiometric calibration. The candidate reference image was processed by radiometric calibration and FLAASH atmospheric radiometric correction to obtain the surface reflectance image as the reference image.

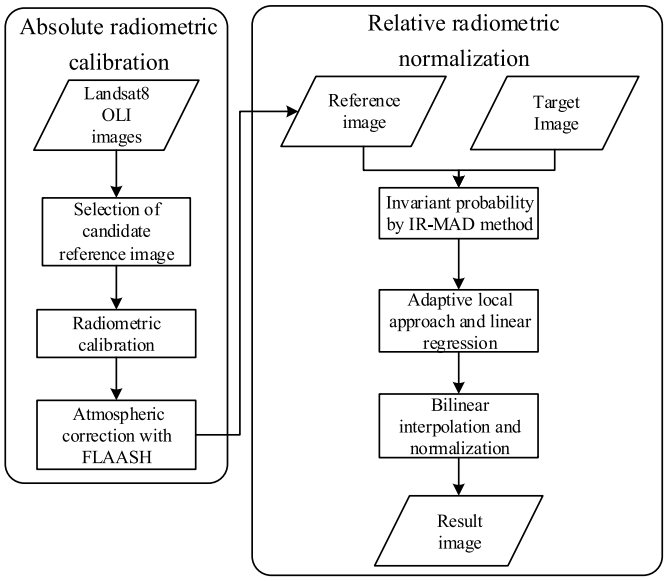

Fig. 1. Flowchart of the MRN approach.

3) Invariant probability of features calculation. The target image was resampled so that its resolution is consistent with that of the reference image. Then, the IR-MAD approach was adopted to calculate the invariant feature probability of each pixel of the target image.
4) Image blocking and calculation of the correction model parameters in each block. The target image was divided into blocks according to the distribution of the ground objects, and the regression coefficients were calculated by a linear regression model.
5) Radiometric normalization. According to the geographic positions of the pixels in the target image, the result image was generated by calibrating each pixel with the calibration parameters using bilinear interpolation.

B. Selection of Candidate Reference Image

As mentioned earlier, the reference image plays an important role in radiometric normalization approaches [30]. Generally, the reference image is selected from the target images in traditional methods. However, the standard for determining the reference image is not unified. In the procedure of aerial triangulation, the control points are employed to restrict the geographic coordinates of the image points [31]. Inspired by this view, the image with right radiometric information can also be employed as the control information for radiometric normalization methods. Therefore, we selected the image which contains the right radiometric information as the reference image.

The surface reflectance products are the real reflection of the surface objects. In other words, the surface reflectance products contain the right radiometric information, which means that they can be selected as the reference images for radiometric normalization methods. In fact, most of the surface reflectance products come from the images after the absolute radiometric normalization. Hence, the images which meet the requirement of absolute radiometric normalization method can be selected as the candidate reference data sets. Then,

TABLE I
IMAGING CHARACTERISTIC OF MULTISPECTRAL SENSOR

Sensor		ZY3	GF-1	GF-2	Landsat 8
Band and Spectral Range /μm	B	0.45~0.52	0.45~0.52	0.45~0.52	0.45~0.51
	G	0.52~0.59	0.52~0.59	0.52~0.59	0.53~0.59
	R	0.63~0.69	0.63~0.69	0.63~0.69	0.64~0.67
	NR	0.77~0.89	0.77~0.89	0.77~0.89	0.85~0.88
Swath/km		51	60(double camera)	45(double camera)	185
Spatial resolution/m		6	8	4	30
Radiometric resolution/bit		10	10	10	12
Recycle/d		5	4	5	16

the factors of geographical coverage, acquisition time, and spatial resolution of the target images were extracted. Next, the image in the candidate reference data sets with the same geographic coverage, acquisition season, and the closest spatial resolution compared with the target images, was selected as the final candidate reference image.

In this paper, Operational Land Imager (OLI) images of Landsat 8 were employed as candidate reference images in the experiments. The reasons are as follows: 1) since the image product of Landsat 8 satellite is open source, it is convenient to obtain the data covering the same area with the target image; 2) research and processing techniques based on Landsat 8 images are mature, and image processing software such as ENVI 5.1 (Exelis-Visual Information Solutions) software has developed an absolute radiometric calibration module for Landsat 8 images; and 3) the OLI images of Landsat 8 are widely covered and have a similar spectral range with many satellite images (such as ZY-1, GF-1, and GF-2 images, see Table I).

C. Absolute Radiometric Calibration for Reference Image

The radiometric calibration as well as the FLAASH calibration module in ENVI 5.1 was adopted in our experiments. First, with the help of radiometric calibration module in ENVI 5.1, the DN value of the Landsat-8 OLI image was transformed into the atmospheric top reflectance value. Then, the FLAASH calibration module in ENVI 5.1 was implemented by fitting to the sensor specifications and some other characteristics (such as area, season, and ground elevation) of the Landsat-8 OLI image, which can convert the atmospheric top reflectance value to surface reflectance.

In order to verify the accuracy of the absolute calibration results, accuracy verification of the calibration result was performed referencing the MODIS surface reflectance product MOD09GA [32], [33]. The MOD09GA product, which is performed with a greater degree of robustness than Landsat images and is easily available [12], [32], is used for the accuracy assessment of the Landsat TM/ETM+ surface reflectance data after absolute atmospheric correction in The Landsat Ecosystem Disturbance Adaptive Processing System team [32], [33]. Since approaches evaluating absolute radiometric calibration results using the reference of MODIS data have been discussed in [32], a simple introduction is made here only.

TABLE II
SIX MULTISPECTRAL BANDS OF THE LANDSAT-8 OLI AND THE CORRESPONDING MODIS BANDS

Landsat8 OLI (band)	OLI bandwidth (nm)	MODIS (band)	MODIS bandwidth (nm)
2	450-510	3	459-479
3	530-590	4	545-565
4	640-670	1	620-670
5	850-880	2	841-876
6	1570-1650	6	1628-1652
7	2110-2290	7	2105-2155

1) For the Landsat-8 OLI image to be verified, the MOD09GA product, acquired on the same date and encompass or intersect with the Landsat image, needs to be identified. The MOD09GA data with sinusoidal projection were reprojected onto the Landsat-8 OLI data's Universal Transverse Mercator Projection by using the nearest neighbor sampling method.
2) For each Landsat-8 OLI image and its simultaneously acquired MOD09GA image, the comparison is performed based on samples. Each sample is a surface reflectance value pair collected from both Landsat and MOD09GA images at the same coordinate and is located in the homogeneous regions in both images.
3) The samples are filtered to exclude nonhomogeneous pixels, pixels contaminated by cloud and shadow, and MOD09GA pixels with view zenith different from Landsat.
4) The accuracy verification is performed by a scatter point display composed of the samples.

Scatter plots provide graphic views of similarity. Since there exist six corresponding bands with similar spectral range between Landsat 8 and MODIS (Table II), the experiment was conducted with six bands. An overall plot was generated by combining all the six spectral bands together. Bands 2–7 represent the corresponding bands in Landsat-8 OLI. In Fig. 2, the x-axis represents the point values of MOD09GA, while the y-axis corresponds to the point values of Landsat-8 OLI data. If the absolute calibration accuracy of Landsat 8 is improved, the scatter plots are linearly distributed and mostly concentrated near the line$y = x$. As shown in Fig. 2, the distribution of scatter plots was linear and close to the line $y = x$, indicating that the calibration results of Landsat-8 OLI were highly consistent with MODIS data.

D. Invariant Probability of Features Calculation With IR-MAD

After obtaining the reference image, the radiometric calibration transformation relationship between the reference image and the target image was established. Among the transformation approaches, a method introducing invariant features into calculation is widely adopted. Generally, the invariant feature extraction method processes data with the same unit, such as two images of DN value or two surface reflectance images.

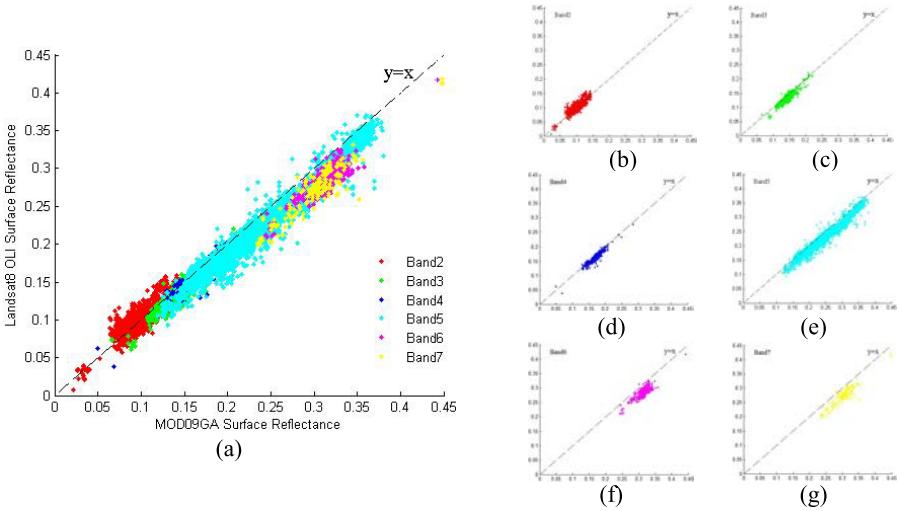

Fig. 2. (a) Scatter plots of overall plot for six spectral bands and (b)–(g) scatter plot of each individual Landsat8 band, where the x-axis represents the point values of MOD09GA, while the y-axis corresponds to the point values of Landsat-8 OLI data. Band2–band7 represent the corresponding bands in Landsat-8 OLI.

However, in the proposed method, the invariant feature was extracted from the surface reflectance image and the DN value image, which means that the test data have different units.

Strictly speaking, the relationship between the DN value and its corresponding surface reflectance is not linear, though the relationship may become linear under certain assumptions. In many cases, when the visibility is high, a linear relationship does exist between the DN value and the surface reflectance, as illustrated in [25]. Since the reference images in the experiments have a good imaging quality and visibility, which meets the above-mentioned requirements, here, we assume that the relationship between the DN value and its corresponding surface reflectance is linear.

Under this assumption, an invariant feature extraction method, which is linear invariant, can be adopted in the process of both the surface reflectance image and the DN value image. Different from the other invariant feature extraction methods, such as the PCA method and the I-SFA method, the MAD approach is invariant to linear and affine scaling [15]. In other words, conducting MAD transformation on images both before and after linear transformation will yield the same result. IR-MAD is the iterative result of MAD, which means that IR-MAD is also invariant to linear and affine scaling. Therefore, the IR-MAD was applied in this paper, where the invariant probability of the corresponding pixel of both the target DN value image and the reference surface reflectance image is extracted.

The invariant feature probability of the pixel extracted by IR-MAD method indicates the probability of no change. In traditional radiometric normalization method, the pixel whose probability of no change is higher than a given threshold (such as 0.85 or 0.95) is selected as an invariant feature point for the radiometric normalization purpose. However, the threshold is empirical, which will affect the results of radiometric calibration [18]. In order to make the radiometric normalization automatically, the invariant feature points were not extracted by setting a threshold in this paper. Instead, all the pixels, whose invariant probability was considered as the weight in further calibration model calculations, were kept in the image.

E. Adaptive Local Approach

Images are generally considered as a whole in the calculation of radiometric calibration in traditional approaches. In other words, only one transformation model exists in an image, leading to neglecting the locality and inhomogeneity of the ground objects distribution. To solve this problem, images were divided into blocks based on the distribution of ground objects in this paper, and the transformation model parameters were calculated in blocks. The block size of an image was relevant to its feature richness, which could be described by the coefficient of variation. The coefficient of variation, meaning the ratio of the standard deviation and average, reflects the discrete degree of data. Unlike the standard deviation, the coefficient of variation is resistant to scale and unit changes. The ratio of the variation coefficient and the reference variation coefficient was then calculated, and the block number was obtained according to the reference variation coefficient. If the mean value and standard deviation corresponding to the reference variation coefficient are 128 and 45, then the reference variation coefficient is 0.352, namely, 45/128. Assuming that the image corresponding to the reference coefficient was divided into $m \times n$ blocks, and then, the target image could be divided into $M \times N$ blocks, calculated by formulas in the following:

$$M = r \times m, N = r \times n \tag{7}$$

$$r = \frac{CA}{CA_{\text{ref}}}, \quad CA = \frac{\sigma}{\mu} \tag{8}$$

where CA is the coefficient of variation, σ is the standard deviation, μ is the mean value, r is the ratio of the variation coefficient, CA_{ref} is the reference variation coefficient, m and n are blocking the number of rows and columns that correspond to the reference variation coefficient, and M and N are the blocking number of the row and column of the target image.

F. Linear Regression

Relative radiometric normalization tends to assume that the radiometric difference between the target image and the reference image can be described by linear difference of the invariant features, as follows:

$$T1_j^i = a_j T2_j^i + b_j \tag{9}$$

where $T1_j^i$ is the gray value of the ith pixel of band j in the image obtained at time 1, $T2_j^i$ is the corresponding gray value in the image obtained at time 2, and a_j and b_j are the linear regression coefficients of band j.

The time 2 image is calibrated based on the time 1 image according to the linear regression coefficients, where $T2_{\mathrm{New}_j^i}$ is the calibrated gray value of $T2_j^i$

$$T2_{\mathrm{New}_j^i} = a_j T2_j^i + b_j. \tag{10}$$

Linear regression coefficients can be calculated by regression models, such as the orthogonal regression (OR) model and the least squares regression (LSR) model. Canty *et al.* [14] considered that the OR model was more applicable than the LSR model in the calculation of radiometric correction regression coefficient. However, Zhang *et al.* [18] found that the LSR model performed better than the OR model. In other words, different researchers get different conclusions in the selection of linear regression model. Therefore, the two models were both tested in this paper to obtain the more suitable model for the proposed method.

The relationship in the LSR model can be described as

$$T2_{\mathrm{New}_j^i} = \frac{\sigma^2_{T1_jT2_j}}{\sigma^2_{T2_j}} \times T2_j^i + \mu_{T1_j} - \frac{\sigma^2_{T1_jT2_j}}{\sigma^2_{T2_j}} \times \mu_{T2_j} \tag{11}$$

where $\sigma^2_{T1_jT2_j}$ is the covariance between images, $\sigma^2_{T2_j}$ is the variance of the time 2 image, μ_{T1_j} is the mean value of the time 1 image, and μ_{T2_j} is the mean value of the time 2 image.

The relationship in the OR model can be described as

$$\begin{aligned} T2_{\mathrm{New}_j^i} &= \frac{(\sigma^2_{T1_j} - \sigma^2_{T2_j}) + \sqrt{(\sigma^2_{T1_j} - \sigma^2_{T2_j})^2 + 4(\sigma^2_{T1_jT2_j})^2}}{2\sigma^2_{T1_jT2_j}} \times T2_j^i \\ &\quad + \mu_{T1_j} - \frac{(\sigma^2_{T1_j} - \sigma^2_{T2_j}) + \sqrt{(\sigma^2_{T1_j} - \sigma^2_{T2_j})^2 + 4(\sigma^2_{T1_jT2_j})^2}}{2\sigma^2_{T1_jT2_j}} \\ &\quad \times \mu_{T2_j}. \end{aligned} \tag{12}$$

G. Bilinear Interpolation for Correction Parameters

Our regression models were built by considering the invariant probability as the weight for each pixel in the block according to the blocking result (Fig. 3). In this way, the radiometric calibration parameters could be obtained. For an image divided into $M \times N$ blocks, $M \times N$ groups of radiometric calibration parameters were obtained. To avoid the blocking effect, weighted bilinear interpolation was adopted to calculate the calibration parameters of each pixel. Then, each pixel was calibrated to generate the normalization result

$$C(i, j) = \overrightarrow{C_B} \cdot \overrightarrow{P} \tag{13}$$

$$\overrightarrow{C_B} = (C_B(w, v), \quad C_B(w \pm 1, v), \quad C_B(w, v \pm 1), \quad C_B(w \pm 1, v \pm 1)) \tag{14}$$

$$\overrightarrow{P} = (P(w, v), \quad P(w \pm 1, v), \quad P(w, v \pm 1), \quad P(w \pm 1, v \pm 1)) \tag{15}$$

where $C(i, j)$ is the radiometric calibration parameter of pixel (i, j); (w, v) is the block of pixel (i, j), $w \in M, v \in N$; $\overrightarrow{C_B}$ is the radiometric correction coefficient vector; $C_B(w, v)$ is the calibration parameter of block (w, v); the same goes for $C_B(w \pm 1, v)$, $C_B(w, v \pm 1)$, and $C_B(w \pm 1, v \pm 1)$, where $\pm$ is relevant to the position of the pixel in the block, $\overrightarrow{P}$ is the weight vector corresponding to $\overrightarrow{C_B}$, and the weight is inversely proportional to the distance.

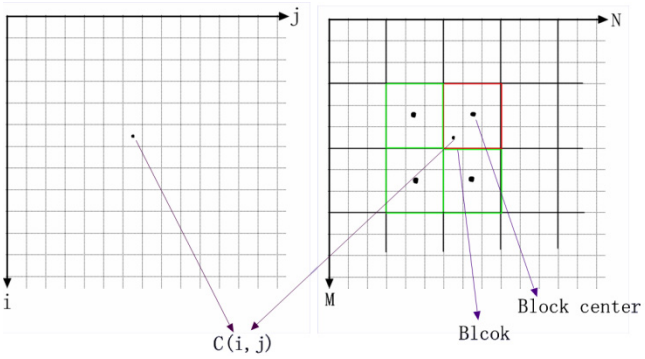

Fig. 3. Bilinear interpolation schemes.

TABLE III
BASIC INFORMATION OF EXPERIMENT DATA SETS

Dataset	Image ID	Sensor Type	GSD/m	Swath /Km	Acquisition Time
1	1	GF-1	8	36	2013.11.30
	2	GF-1	8	36	2013.11.30
	3	GF-1	8	36	2013.12.12
	4	GF-1	8	36	2013.12.12
	Reference	Landsat 8	30	180	2013.12.10
2	1	ZY-3	6	51	2013.04.07
	2	ZY-3	6	51	2013.04.07
	3	ZY-3	6	51	2012.10.17
	4	ZY-3	6	51	2012.10.17
	Reference	Landsat 8	30	180	2013.10.14
3	1	ZY-3	6	51	2013.03.13
	2	ZY-3	6	51	2013.03.13
	3	GF-1	8	36	2014.02.20
	4	GF-1	8	36	2014.02.20
	5	GF-1	8	36	2014.02.20
	Reference	Landsat 8	30	180	2014.03.14
4	1	GF-2	1	23	2015.02.17
	2	GF-2	1	23	2015.02.17
	3	GF-2	1	23	2014.12.25
	4	GF-2	1	23	2014.12.25
	Reference	Landsat 8	30	180	2015.02.11

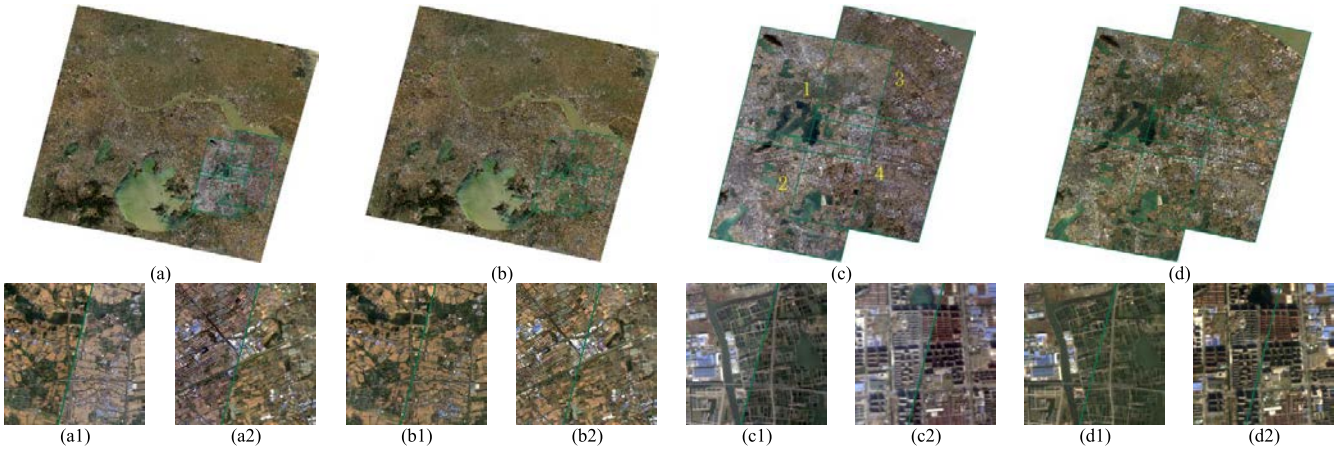

Fig. 4. Comparison between the images before and after radiometric normalization in the first data set. (a) Overlaid image before normalization. (a1) and (a2) Detail areas marked by red box in (a). (b) Overlaid image after normalization. (b1) and (b2) Corresponding detail areas of (a1) and (a2) in (b). (c) Mosaic image of the target images before normalization. (c1) and (c2) Detail areas marked by red box in (c). (d) Mosaic image of the target images after normalization. (d1) and (d2) Corresponding detail areas of (c1) and (c2) in (d). Green lines in the above images are the boundaries of the target images.

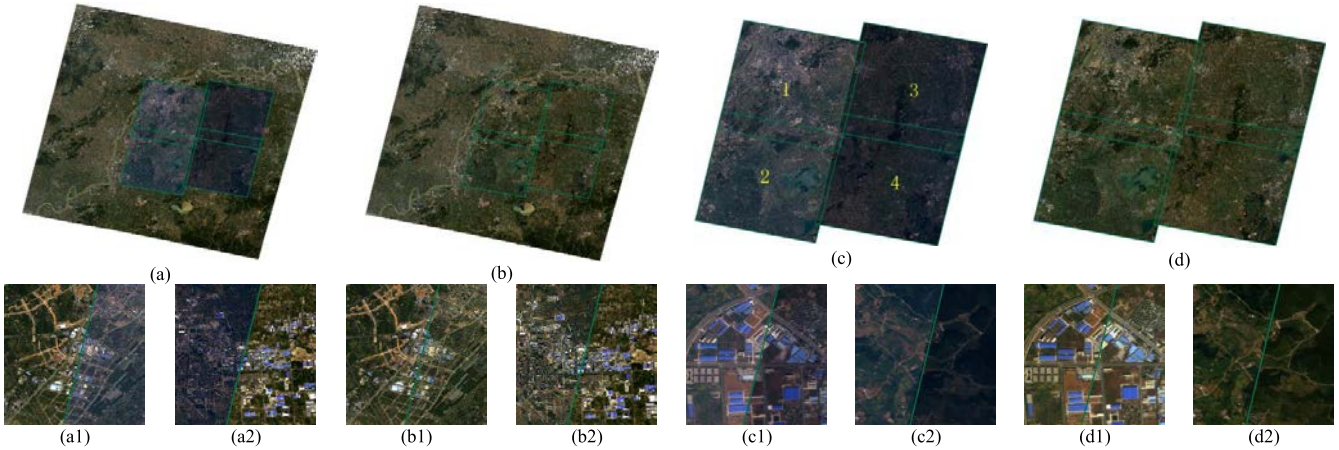

Fig. 5. Comparison between the images before and after radiometric normalization in the second data set. (a) Overlaid image before normalization. (a1) and (a2) Detail areas marked by red box in (a). (b) Overlaid image after normalization. (b1) and (b2) Corresponding detail areas of (a1) and (a2) in (b). (c) Mosaic image of the target images before normalization. (c1) and (c2) Detail areas marked by red box in (c). (d) Mosaic image of the target images after normalization. (d1) and (d2) Corresponding detail areas of (c1) and (c2) in (d). Green lines in above images are the boundaries of the target images.

IV. Results and Analysis

A. Study Data

Multispectral images from ZY-3, GF-1 satellites, and the fused images (the adopted fusion approach effectively combines the spatial and spectral characteristics of the original images) from the GF-2 satellite of China were used as experimental data. The spatial resolutions are 6, 8, and 1 m, respectively. ZY-3, launched on January 9, 2012, is the first civilian high-resolution stereo mapping satellite in China; GF-1 is the first satellite of the high-resolution land-observation system of China, launched on April 26, 2013; GF-2 is the first civilian satellite with the resolution better than 1 m in China launched on August 19, 2014. As mentioned earlier, the OLI images of Landsat 8 were employed as reference images in the experiments of this paper.

Four data sets shown in Table III and Figs. 4–7 were selected for experimentation and analysis. Each experiment data set was orthorectified to the same resolution with control points and digital elevation model, and the root-mean-square error (RMSE) was less than 0.5 pixels. The World Geodetic System 84 datum with the longitude and latitude coordinates was used in all images [14], [15], [28]. Then, the reference images were matched to the target images with an RMSE less than 15 m (0.5 pixels of the reference image). Geometric corrections have been developed for both coarse and fine resolution satellite data [10], which will not be discussed further here. Though the proposed method can deal with images with any number of bands, three bands of the image were selected for the experiments, as display devices can only show three bands. And the R-, G-, and B-bands are selected since a true color image consistent with human cognition can be formed by combining corresponding bands.

B. Visual Assessments

The above-mentioned four data sets were normalized by the proposed method, and each image was divided in 6×6 blocks and processed by the LSR model; the results are shown in Figs. 4–7. It is worth noting that although the 16-b images were used in the experiment, they were compressed to 8 b for the purpose of display. The experimental results were displayed in true color and each data set is stretched to an

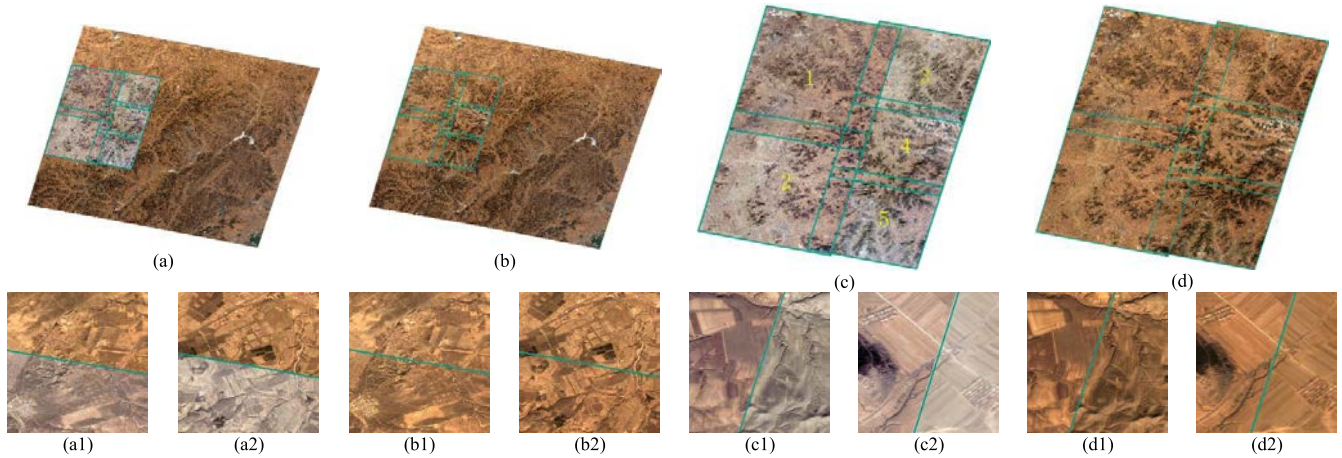

Fig. 6. Comparison between the images before and after radiometric normalization in the third data set. (a) Overlaid image before normalization. (a1) and (a2) Detail areas marked by red box in (a). (b) Overlaid image after normalization. (b1) and (b2) Corresponding detail areas of (a1) and (a2) in (b). (c) Mosaic image of the target images before normalization. (c1) and (c2) Detail areas marked by red box in (c). (d) Mosaic image of the target images after normalization. (d1) and (d2) Corresponding detail areas of (c1) and (c2) in (d). Green lines in above images are the boundaries of the target images.

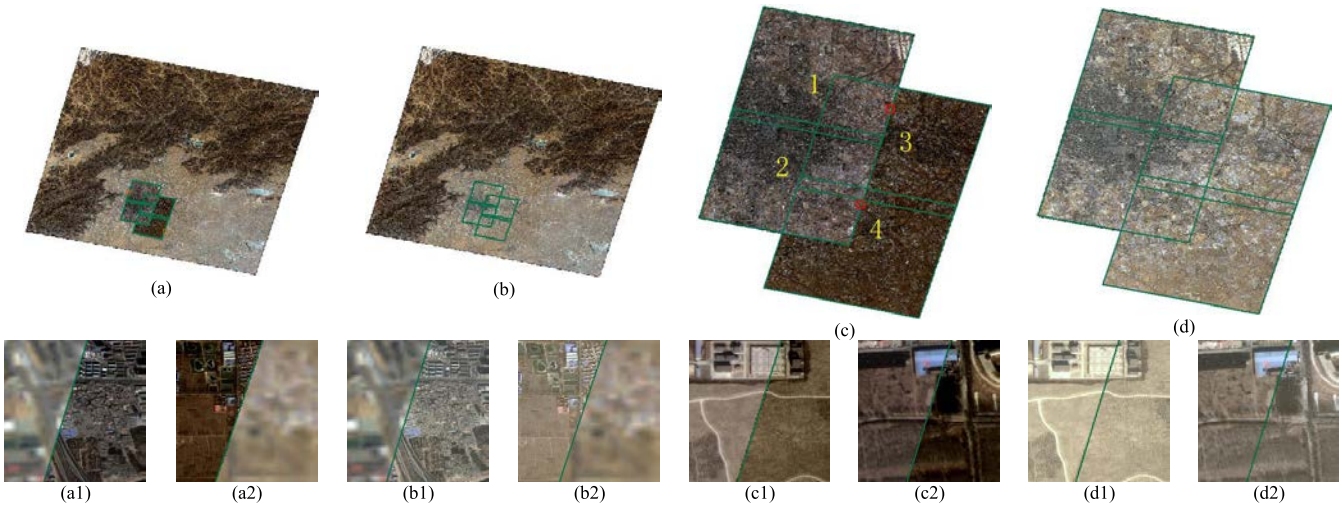

Fig. 7. Comparison between the images before and after radiometric normalization in the fourth data set. (a) Overlaid image before normalization. (a1) and (a2) Detail areas marked by red box in (a). (b) Overlaid image after normalization. (b1) and (b2) Corresponding detail areas of (a1) and (a2) in (b). (c) Mosaic image of the target images before normalization. (c1) and (c2) Detail areas marked by red box in (c). (d) Mosaic image of the target images after normalization. (d1) and (d2) Corresponding detail areas of (c1) and (c2) in (d). Green lines in above images are the boundaries of the target images.

8-b image according to the same threshold of its corresponding reference image.

Four data sets before and after radiometric normalization were overlaid with the reference images for comparison, as shown in Figs. 4(a) and (b)–7(a) and (b). Figs. 4(a)–7(a) are the overlaid images of the target images before normalization and the reference images. The areas marked by green lines are the images to be corrected and the base images are the reference images. It can be seen that obvious radiometric differences exist between the target and the reference images. In contrast, Figs. 4(b)–7(b) are the overlaid images of the corrected images and the reference images, from which no obvious radiometric differences can be seen. The detailed comparison between (a1) and (b1) and (a2) and (b2) from corresponding areas in the red box in (a) and (b) is shown in Figs. 4–7. These details further indicate that no obvious radiometric differences exist between the corrected images and the reference images.

The four data sets before and after radiometric correction were compared in Figs. 4(c) and (d)–7(c) and (d), from which it can be inferred that radiometric differences exist between these images in varying degrees. However, there are no obvious differences between the mosaic images after normalization in Figs. 4(d)–7(d). (c1), (c2), (d1), and (d2) of Figs. 4–7 compared the details corresponding to the areas in the red box in (c) and (d). These details further indicate that there are no obvious radiometric differences between the target images after correction.

In the four data sets, the reference image and the image to be corrected shared the same geographical coverage and the overlapping area is the target image itself, which is independent of the overlapping relationship between the target images. The third set of images is heterologous, which makes radiometric correction more difficult than for homologous images. From Fig. 6, it can be seen that after correcting by the proposed method, the radiometric differences between the experiment

TABLE IV
EVALUATION COMPARISON OF THE NORMALIZATION RESULT OF THE FIRST EXPERIMENT DATA SET UNDER DIFFERENT METHODS

			OR				LSR			
	METHOD / BAND	ORIGIN	IR-MAD_0.95	MRN_A1	MRN__A3	MRN__A6	IR-MAD_0.95	MRN_A1	MRN__A3	MRN__A6
RMSE	1	4.6010	1.0933	1.0927	1.0839	1.0788	1.0934	1.0927	1.0822	**1.0769**
	2	1.9033	0.6303	0.6302	0.6304	0.6280	0.6303	0.6267	0.6265	**0.6234**
	3	6.6659	1.7672	1.7706	1.7569	1.7481	1.7660	1.7539	1.7389	**1.7302**
ED		4.7598	0.9711	0.9728	0.9630	0.9539	0.9705	0.9646	0.9540	**0.9452**

TABLE V
EVALUATION COMPARISON OF THE NORMALIZATION RESULT OF THE SECOND EXPERIMENT DATA SET UNDER DIFFERENT METHODS

			OR				LSR			
	METHOD / BAND	ORIGIN	IR-MAD_0.95	MRN_A1	MRN__A3	MRN__A6	IR-MAD_0.95	MRN_A1	MRN__A3	MRN__A6
RMSE	1	3.0794	1.3799	1.3787	1.3721	1.3716	1.3903	1.3846	1.3670	**1.3653**
	2	1.0212	0.9433	0.9414	0.9396	0.9388	0.9728	0.9648	0.9334	**0.9319**
	3	6.3830	1.9091	1.9077	1.9053	1.9078	1.9117	1.9032	**1.8955**	1.8971
ED		4.1021	1.0566	1.0552	1.0493	1.0481	1.0614	1.0544	1.0421	**1.0403**

image and the reference image are basically eliminated, and subsequently, there are no radiometric differences among the target images. Located in Beijing, China with the spatial resolution of 1 m, the fourth data set is a complex area of high-rise buildings. However, the proposed can still yield good results. All the above-mentioned results demonstrate that the proposed method not only applies to homologous images, but also works well for heterologous images.

C. Statistical Analysis

Visual assessment is usually conducted on display devices which rely on RGB color space. However, the RGB color space is not uniform and is nonlinear, which does not conform to the human visual system. For example, four digital color values exist in a channel in RGB color space, namely, $\upsilon 1 = 30$, $\upsilon 2 = 40$, $\upsilon 3 = 200$, and $\upsilon 4 = 210$. Although the difference between the values are the same ($\upsilon 2 - \upsilon 1 = 10 = \upsilon 4 - \upsilon 3$), the difference in color perceived by humans may vary because of the nonlinear RGB color space. Therefore, it is very likely that the results of subjective assessment are inconsistent with that of objective assessment in RGB color space.

Given that RGB color space is not uniform, CIELAB color space was adopted to evaluate the results quantitatively. CIELAB color space, one of the most comprehensive color models describing colors in human vision, is an approximately uniform color space independent of display devices [34]. The objective metrics of Euclidean distance (ED) and RMSE are used to evaluate the results quantitatively.

1) ED: The relative perception difference between any two colors in CIELAB color space can be calculated by the ED between the three-color components (L^*, a^*, b^*) of each color. Therefore, ED was adopted to measure the difference between images. A small value indicates a close relationship in information between images

$$\Delta E_{ab} = \frac{\sum_{i=1}^{n} \sqrt{(L_2^* - L_1^*)^2 + (a_2^* - a_1^*)^2 + (b_2^* - b_1^*)^2}}{n} \tag{16}$$

where (L_1^*, a_1^*, b_1^*) and (L_2^*, a_2^*, b_2^*) are two colors in CIELAB space.

2) RMSE: RMSE is a commonly applied evaluation index in describing the difference between the reference image and the target image. A small value indicates a close relationship between them [35]

$$\text{RMSE} = \sqrt{\frac{\sum_{i=1}^{n} (\text{Val}_{R_i} - \text{Val}_{T_i})^2}{n}} \tag{17}$$

where n is the pixel number, Val_{R_i} is the gray value of the ith pixel in the reference image, and Val_{T_i} is the corresponding calibrated value.

The proposed approach was evaluated by quantitatively analyzing and contrasting it with other methods. In order to analyze the influence of the blocking size in the proposed method, three cases were considered. First, every target image was divided into one block (i.e., $M = 1$ and $N = 1$), and the proposed method under this situation is called MRN_A1. Second, every target image was divided into 3×3 blocks (i.e.,$M = 3$ and $N = 3$), and the proposed method under this situation is called MRN_A3. Third, every target image was divided into 6×6 blocks (i.e.,$M = 6$ and $N = 6$), and the proposed method under this situation is called

TABLE VI
EVALUATION COMPARISON OF THE NORMALIZATION RESULT OF THE THIRD EXPERIMENT DATA SET UNDER DIFFERENT METHODS

			OR				LSR			
	METHOD / BAND	ORIGIN	IR-MAD_0.95	MRN_A1	MRN__A3	MRN__A6	IR-MAD_0.95	MRN_A1	MRN__A3	MRN__A6
RMSE	1	3.8997	1.2530	1.2518	1.2525	1.2510	1.2528	1.2481	1.2482	**1.2453**
	2	2.1434	0.7195	0.7184	0.7093	0.7048	0.7192	0.7149	0.7056	**0.7000**
	3	7.6973	2.0037	2.0021	2.0007	2.0008	2.0030	1.9918	1.9868	**1.9833**
ED		5.0621	1.0543	1.0531	1.0470	1.0428	1.0539	1.0485	1.0411	**1.0357**

TABLE VII
EVALUATION COMPARISON OF THE NORMALIZATION RESULT OF THE FOURTH EXPERIMENT DATA SET UNDER DIFFERENT METHODS

			OR				LSR			
	METHOD / BAND	ORIGIN	IR-MAD_0.95	MRN_A1	MRN__A3	MRN__A6	IR-MAD_0.95	MRN_A1	MRN__A3	MRN__A6
RMSE	1	15.3077	0.8937	0.8918	0.8911	0.8896	0.8896	0.8826	0.8794	**0.8752**
	2	10.4330	0.3557	0.3538	0.3484	0.3464	0.3553	0.3508	0.3447	**0.3424**
	3	13.1426	1.7624	1.7516	1.7463	1.7434	1.7597	1.7328	1.7231	**1.7170**
ED		22.5861	1.4236	1.4236	1.4178	1.4139	1.4096	1.4216	1.4044	**1.3970**

MRN_A6. Moreover, the conventional IR-MAD with 0.95 as the threshold, or IR-MAD_0.95, was used as the contrast method. In order to analyze the influence of the linear regression models on the normalization results, the LSR and OR models were both tested. Four sets of data were processed by the above-mentioned four methods and statistical analysis was conducted. The statistical results are shown in Tables IV–VII. The column corresponding to LSR and OR in the table IV-VII represents the evaluation of the image processed by the LSR and OR models, respectively; the column of Origin represents the evaluation of the original images; and the method row represents the adopted method. In addition, the numbers marked as bold and underline are the minimum value in each row.

Tables IV–VII show that the RMSE and ED of MRN_A6 are the smallest in most cases, which indicates that MRN_A6 works well for normalization and that the LSR regression model performed better. The evaluation values of both the LSR model and OR model presented a gradually decreasing trend from left to right, revealing that their correction results improve gradually from left to right. In other words, the results of MRN_A1 are better than those of IR-MAD_0.95, the results of MRN_A3 are better than those of MRN_A1, and the results of MRN_A6 are better than those of MRN_A3. All the results demonstrate that the proposed method (MRN), when all the pixels in the image are given weights according to their constant probabilities to participate in the subsequent correction model, produced better results than the method of extracting invariable features by specifying the threshold artificially. The results also indicate that the proposed block correction method is more applicable to high-resolution images. It is also shown that both the LSR and OR correction models can be applied to the proposed method, but the LSR model is more effective in general.

V. DISCUSSION

The novel MRN method proposed in this paper combines the absolute and relative radiometric normalization methods to eliminate the radiometric difference in high-resolution image mosaicking. The differences as well as improvements of the proposed approach compared with the traditional approaches are specified as follows.

First, the types of study objects are different. Most of the existing methods [1], [2], [3], [10], [14], [18], [23], take medium-resolution images, such as Landsat TM or HJ-1A images as the test data. The objects of study in this paper consist of medium- and high-resolution data, by which the characteristics of both images are taken into consideration. High-resolution imagery plays an increasingly important role in remote sensing application. However, the research of high-resolution satellite imagery in radiometric normalization method for mosaicking is not mature enough to match its significant role in land use and other applications. Therefore, the research about high-resolution imagery in this paper is necessary.

Second, the way of selecting reference image is different. The reference image, needed in most radiometric normalization methods, provides the radiometric information for the target images to be adjusted. For most of the existing radiometric calibration approaches, the standard to determine reference image is not unified, thus yielding different calibration results. However, the proposed approach regards surface

reflectance products after absolute radiometric correction as the reference image. The surface reflectance products present the true reflectance characteristics of features which are almost equivalent to the true reference values. Hence, the problem of choosing the reference image in traditional methods is solved. Besides, to a certain degree, choosing the surface reflectance product as the reference to correct other images reduces the influences caused by the atmosphere and other factors which make up for the limitation of absolute calibration of high-resolution images.

Third, the processing workflow is different. Most of the existing methods can process only a single pair of test images at a time, namely, one image in the pair is set as the reference for the other one to match to. The matched image will be the reference in the next pair and the rest can be processed in the same manner. So in most cases, the test data will be corrected sequentially which will slow down the process and bring the risk of color error propagation. Besides, Guindon's investigation [36] shows that different sequential paths may generate different results. However, for the proposed method, the selected reference data have the same geographic coverage with the target images, which means each target image has its own geography-related reference data [as shown in Figs. 4(a) and (b)–7(a) and (b)]. Therefore, the target images can be corrected independently and no sequential relationship exists among the processing procedures, thus avoiding the two-body problem effectively and contributing to parallel processing. As mentioned earlier, the number and quality of the pseudoinvariant features in overlapping areas play an important role in generating calibration results. Generally speaking, a larger scale of overlapping area and a great number of pseudoinvariant features indicate a high precision of pseudoinvariant feature extraction, and vice versa. In conventional methods, a single pair of adjacent test images is processed at a time. When the overlapping rate of the image pair is low or great changes in features have taken place, the extraction results of pseudoinvariant features in the overlapping areas may be incorrect and may lead to the wrong normalization results. However, in the proposed method, the geographical coverage of the reference image completely covers that of the target image; that is, the overlapping area is the target image itself, bringing great advantages in extracting invariable features. The images to be corrected are independent so that color transfer is unnecessary among neighboring target images. Correction based on geographical position fully considers the spatial distribution of features. Hence, the correction results are more consistent with the actual conditions. In addition, no sequential relationship exists among the processing procedures, thus avoiding the two-body problem effectively and contributing to parallel processing.

Fourth, the number of regression model is different. Images are generally considered as a whole in the process of radiometric normalization in traditional approaches. In other words, only one transformation model exists in an image, which may result in the neglect of locality and inhomogeneity of the ground object distributions especially for the high-resolution images. High-resolution images could present the ground features more clearly, and the disparity between features is more obvious. Because of the uneven distribution of features, the different regions of image may have different radiometric characteristics, such as the farmland and the city. The adaptive local correction strategy processes the image block by block and builds the regression model in conformity with its feature characteristics, by which the correction results can be generated. The blocking strategy is able to take the feature distribution into account, which is beneficial to the correction of high-resolution images. Besides, the IR-MAD algorithm used in traditional methods extracts pseudoinvariant features with a certain empirical threshold which may result in different results with different values. In contrast, all pixels with their weights which are extracted by the IR-MAD algorithm are used to participate in building the regression model in the proposed method. In this way, not only is it unnecessary to specify the threshold to increase the level of automation, but the characteristics of the feature distribution are also better reflected, contributing to eliminating the radiometric differences among the images.

The experimental results demonstrate that the proposed method can correct both homologous and heterologous high-resolution images. The radiometric differences are not only eliminated between the target image and the reference image, but also eliminated between the target images, which brings great contribution to image mosaicking. The quantitative analysis, which is quantitatively evaluated in CIELAB color space, shows that the proposed method achieved better results than the conventional IR-MAD method; the comparison of different parameters indicates that all the improvements in the proposed method are effective.

It is worth to note that the reference image plays an important role in the proposed MRN method. In our experiment, we have proved that for images with 8, 6, and 1 m resolution, satisfactory results can be yielded by referencing the 30-m-resolution image. However, the performance of the proposed approach remains uncertain for a higher resolution target image such as 0.1 m by referencing a 30-m-resolution image. The impact of resolution differences between the reference and target images is twofold. On the one hand, due to the limitation of the charge-coupled device frame, the coverage of the image will decrease as the resolution increases. A small geographical coverage indicates that the number of corresponding pixels between the high-resolution target image and the medium-resolution reference image becomes small, which is adverse to the extraction of pseudoinvariant features relatively. On the other hand, the transformation relationship in radiometric information between the target image and the reference image is the reflection of the difference of pseudoinvariant features which is extracted pixel-to-pixel. A pixel in the medium-resolution image is the generalization of several pixels of the same area in the high-resolution target image. When the resolution difference between the two images exceeds a certain range, the down-sampled pixels of the high-resolution target image cannot represent the corresponding pixel after image generalization. Therefore, it can be concluded that the accuracy of the calibration result tends to reduce as the difference between the target image and the reference image becomes bigger. In order to verify the assumption, the fourth experi-

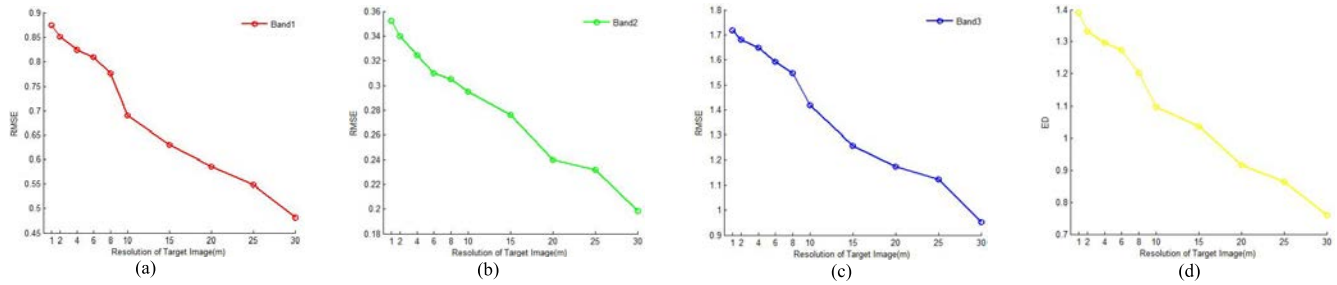

Fig. 8. Accuracy trend of the normalization results generated by different target images of different resolutions with the same reference image. The *x*-axis represents the resolution of target images, while the *y*-axis corresponds to the values of RMSE or ED. The accuracy increases as the value of RMSE or ED becomes smaller.

mental data were used for simulation. The 1-m-resolution data were resampled to 2, 4, 6, 8, 10, 15, 20, 25, and 30 m, respectively. The resampled images were normalized by the proposed method with the same 30-m-resolution reference image. Each image was divided into blocks and processed by the LSR model. The statistical results are shown in Fig. 8. It can be inferred that the accuracy of the calibration results will increase as the resolution difference between the target and reference images reduces and vice versa, which is consistent with the above-mentioned assumption. Therefore, the resolution difference between the reference and target images should be restricted in a reasonable range to get a good calibration result. In this paper, it is proved that the reference image with the resolution of 30 m can be applied to calibrate the target image with the maximum resolution of 1 m. Further experiment is needed to verify whether the target image with very high-resolution ($<$ 1 m) can still be normalized well with the 30-m-resolution reference image. However, it could be predicted that a good normalization result will be generated when the resolution difference between the reference and target images is suitable.

VI. Conclusion

Radiometric differences always exist among high-resolution images with a different time lapse in image mosaicking. The combined radiometric correction method proposed in this paper aims to eliminate the influence of the radiometric differences on the mosaic results. In order to provide an improved approach to radiometric correction for the image mosaicking purpose, the proposed method combines both the accuracy of the absolute radiometric correction and the flexibility of the relative radiometric correction, while avoiding their disadvantages at the same time. Interferences brought by the atmosphere and other factors are eliminated in the reference image after absolute radiometric correction, from which the real reflectance characteristics of features can be references when correcting high-resolution images, thus giving the relative radiometric correction physical meaning and guaranteeing the uniqueness of the reference image. In addition, the medium-resolution images and the high-resolution images to be corrected share the same geographical coverage. On the one hand, in the correction of high-resolution images, the entire information of the image can be taken into consideration, thus avoiding the limitation of determining correction factors by the overlapping area only in conventional relative radiation correction approaches. On the other hand, the images to be corrected are independent so that they can be processed in parallel, by which the two-body problem can be effectively avoided. Given the complex features and their uneven distribution in high-resolution images, the adaptive local correction strategy processes the image block-by-block, improving the results effectively.

The experiments conducted using four data sets demonstrated that the proposed method can correct both the homologous and heterologous images. The radiometric information of the corrected images is similar to that of the reference image, which shows that the influences of the atmosphere and other factors were also reduced in the correction. The quantitative analysis indicates that the proposed method remarkably improved the results of the original IR-MAD method, and that all the improvements were effective. Moreover, the experiments demonstrated that both the LSR and OR models are applicable to the proposed method, between which the former performed better.

Acknowledgment

The authors would like to thank the editor and reviewers for their instructive comments that helped improve this paper. They would also like to thank the International Scientific Data Service Platform and the Image Sky Company of Suzhou for providing experimental data sets.

References

[1] F. Gao, J. G. Masek, R. E. Wolfe, and C. Huang, "Building a consistent medium resolution satellite data set using moderate resolution imaging spectroradiometer products as reference," *J. Appl. Remote Sens.*, vol. 4, no. 1, p. 043526, Apr. 2010.

[2] I. Olthof, D. Pouliot, R. Fernandes, and R. Latifovic, "Landsat-7 ETM+ radiometric normalization comparison for northern mapping applications," *Remote Sens. Environ.*, vol. 95, no. 3, pp. 388–398, Apr. 2005.

[3] Y. Du, J. Cihlar, J. Beaubien, and R. Latifovic, "Radiometric normalization, compositing, and quality control for satellite high resolution image mosaics over large areas," *IEEE Trans. Geosci. Remote Sens.*, vol. 39, no. 3, pp. 623–634, Mar. 2001.

[4] C. Chen, Z. Chen, M. Li, Y. Liu, L. Cheng, and Y. Ren, "Parallel relative radiometric normalisation for remote sensing image mosaics," *Comput. Geosci.*, vol. 73, pp. 28–36, Dec. 2014.

[5] X. Chen, L. Vierling, and D. Deering, "A simple and effective radiometric correction method to improve landscape change detection across sensors and across time," *Remote Sens. Environ.*, vol. 98, no. 1, pp. 63–79, Sep. 2005.

[6] L. Paolini, F. Grings, J. A. Sobrino, J. C. J. Muñoz, and H. Karszenbaum, "Radiometric correction effects in Landsat multi-date/multi-sensor change detection studies," *Int. J. Remote Sens.*, vol. 27, no. 4, pp. 685–704, 2006.

[7] C. Song, C. E. Woodcock, K. C. Seto, M. P. Lenney, and S. A. Macomber, "Classification and change detection using Landsat TM data: When and how to correct atmospheric effects?" *Remote Sens. Environ.*, vol. 75, no. 2, pp. 230–244, Feb. 2001.

[8] W. B. Cohen *et al.*, "Comparisons of land cover and LAI estimates derived from ETM+ and MODIS for four sites in North America: A quality assessment of 2000/2001 provisional MODIS products," *Remote Sens. Environ.*, vol. 88, no. 3, pp. 233–255, Dec. 2003.

[9] P. Coppin, I. Jonckheere, K. Nackaerts, B. Muys, and E. Lambin, "Digital change detection methods in ecosystem monitoring: A review," *Int. J. Remote Sens.*, vol. 25, no. 9, pp. 1565–1596, May 2004.

[10] Y. Du, P. M. Teillet, and J. Cihlar, "Radiometric normalization of multitemporal high-resolution satellite images with quality control for land cover change detection," *Remote Sens. Environ.*, vol. 82, no. 1, pp. 123–134, Sep. 2002.

[11] J. O'Connell, J. Connolly, E. F. Vermote, and N. M. Holden, "Radiometric normalization for change detection in peatlands: A modified temporal invariant cluster approach," *Int. J. Remote Sens.*, vol. 34, no. 8, pp. 2905–2924, Jan. 2013.

[12] S. M. Vicente-Serrano, F. Pérez-Cabello, and T. Lasanta, "Assessment of radiometric correction techniques in analyzing vegetation variability and change using time series of Landsat images," *Remote Sens. Environ.*, vol. 112, no. 10, pp. 3916–3934, Oct. 2008.

[13] M. S. Moran and R. D. Jackson, "Evaluation of simplified procedures for retrieval of land surface reflectance factors from satellite sensor output," *Remote Sens. Environ.*, vol. 41, nos. 2–3, pp. 169–184, Aug./Sep. 1992.

[14] M. J. Canty, A. A. Nielsen, and M. Schmidt, "Automatic radiometric normalization of multitemporal satellite imagery," *Remote Sens. Environ.*, vol. 91, nos. 3–4, pp. 441–451, Jun. 2004.

[15] T. A. Schroeder, W. B. Cohen, C. Song, M. J. Canty, and Z. Yang, "Radiometric correction of multi-temporal Landsat data for characterization of early successional forest patterns in western Oregon," *Remote Sens. Environ.*, vol. 103, no. 1, pp. 16–26, Jul. 2006.

[16] N. Bao, A. M. Lechner, A. Fletcher, A. Mellor, D. Mulligan, and Z. Bai, "Comparison of relative radiometric normalization methods using pseudo-invariant features for change detection studies in rural and urban landscapes," *J. Appl. Remote Sens.*, vol. 6, no. 1, p. 063578, Sep. 2012.

[17] M. M. Rahman, G. J. Hay, I. Couloigner, B. Hemachandran, and J. Bailin, "An assessment of polynomial regression techniques for the relative radiometric normalization (RRN) of high-resolution multitemporal airborne thermal infrared (TIR) imagery," *Remote Sens.*, vol. 6, no. 12, pp. 11810–11828, Nov. 2014.

[18] L. Zhang, C. Wu, and B. Du, "Automatic radiometric normalization for multitemporal remote sensing imagery with iterative slow feature analysis," *IEEE Trans. Geosci. Remote Sens.*, vol. 52, no. 10, pp. 6141–6155, Oct. 2014.

[19] O. A. de Carvalho *et al.*, "Radiometric normalization of temporal images combining automatic detection of pseudo-invariant features from the distance and similarity spectral measures, density scatterplot analysis, and robust regression," *Remote Sens.*, vol. 5, no. 6, pp. 2763–2794, May 2013.

[20] W. Philpot and T. Ansty, "Analytical description of pseudoinvariant features," *IEEE Trans. Geosci. Remote Sens.*, vol. 51, no. 4, pp. 2016–2021, Apr. 2013.

[21] C.-H. Lin, B.-Y. Lin, K.-Y. Lee, and Y.-C. Chen, "Radiometric normalization and cloud detection of optical satellite images using invariant pixels," *ISPRS J. Photogramm. Remote Sens.*, vol. 106, pp. 107–117, Aug. 2015.

[22] J. Cihlar *et al.*, "From need to product: A methodology for completing a land cover map of Canada with Landsat data," *Can. J. Remote Sens.*, vol. 29, no. 2, pp. 171–186, Apr. 2003.

[23] M. J. Canty and A. A. Nielsen, "Automatic radiometric normalization of multitemporal satellite imagery with the iteratively re-weighted MAD transformation," *Remote Sens. Environ.*, vol. 112, no. 3, pp. 1025–1036, Mar. 2008.

[24] L. P. Hien, D.-S. Kim, Y.-D. Eo, S.-H. Yeon, and S.-W. Kim, "Comparison of radiometric pre-processing methods to detect change using aerial hyperspectral images," *Int. J. Adv. Comput. Technol.*, vol. 4, no. 9, pp. 1–9, May 2012.

[25] C. Hu and P. Tang, "Automatic algorithm for relative radiometric normalization of data obtained from Landsat TM and HJ-1A/B charge-coupled device sensors," *J. Appl. Remote Sens.*, vol. 6, no. 1, p. 063509, Mar. 2012.

[26] L. Garcia-Torres, J. J. Caballero-Novella, D. Gómez-Candon, and A. I. De-Castro, "Semi-automatic normalization of multitemporal remote images based on vegetative pseudo-invariant features," *PLoS ONE*, vol. 9, no. 3, p. e91275, Mar. 2014.

[27] M. W. Matthew *et al.*, "Atmospheric correction of spectral imagery: Evaluation of the FLAASH algorithm with AVIRIS data," in *Proc. Appl. Imag. Pattern Recognit. Workshop*, 2002, pp. 157–163.

[28] Y. Hu, L. Liu, L. Liu, and Q. Jiao, "Comparison of absolute and relative radiometric normalization use Landsat time series images," *Proc. SPIE*, vol. 8006, p. 800616, Nov. 2011.

[29] H. Hotelling, "Relations between two sets of variates," in *Biometrika*. Oxford, U.K.: Oxford Univ. Press, 1936, pp. 321–377.

[30] M. T. Ibrahim, R. Hafiz, M. M. Khan, and Y. Cho, "Automatic selection of color reference image for panoramic stitching," *Multimedia Syst.*, vol. 22, no. 3, pp. 379–392, 2016.

[31] J. Wang, Y. Ge, G. B. M. Heuvelink, C. Zhou, and D. Brus, "Effect of the sampling design of ground control points on the geometric correction of remotely sensed imagery," *Int. J. Appl. Earth Observat. Geoinf.*, vol. 18, pp. 91–100, Aug. 2012.

[32] C. Hu, W. Zhang, Z. Feng, and P. Tang, "Landsat TM/ETM + and HJ-1A/B CCD data automatic relative radiometric normalization and accuracy verification," *J. Remote Sens.*, vol. 18, no. 2, pp. 267–286, 2014.

[33] M. Feng, C. Huang, S. Channan, E. F. Vermote, J. G. Masek, and J. R. Townshend, "Quality assessment of Landsat surface reflectance products using MODIS data," *Comput. Geosci.*, vol. 38, no. 1, pp. 9–22, Jan. 2012.

[34] B. Hill, T. Roger, and F. W. Vorhagen, "Comparative analysis of the quantization of color spaces on the basis of the CIELAB color-difference formula," *ACM Trans. Graph.*, vol. 16, no. 2, pp. 109–154, 1997.

[35] V. J.-D. Tsai and Y.-T. Huang, "Automated image mosaicking," *J. Chin. Inst. Eng.*, vol. 28, no. 2, pp. 329–340, 2005.

[36] B. Guindon, "Assessing the radiometric fidelity of high resolution satellite image mosaics," *ISPRS J. Photogramm. Remote Sens.*, vol. 52, no. 5, pp. 229–243, Oct. 1997.

Yongjun Zhang was born in 1975. He received the B.S., M.S., and Ph.D. degrees from Wuhan University, Wuhan, China, in 1997, 2000, and 2002, respectively.

He is currently a Professor of Photogrammetry and Remote Sensing with the School of Remote Sensing and Information Engineering, Wuhan University. His research interests include space, aerial, and low-attitude photogrammetry; image matching, combined bundle adjustment with multisource data sets, 3-D city reconstruction, and industrial inspection.

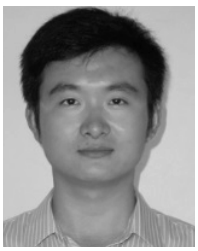

Lei Yu was born in 1989. He received the B.S. degree from Wuhan University, Wuhan, China, in 2011, where he is currently pursuing the Ph.D. degree with the School of Remote Sensing and Information Engineering.

His research interests include cloud detection, image fusion, and radiometric normalization.

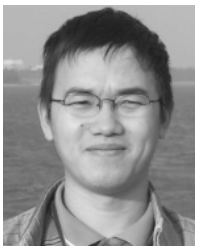

Mingwei Sun was born in 1982. He received the B.S. and Ph.D. degrees from the Wuhan University of Technology, Wuhan, China, in 2004 and 2009, respectively.

He is currently a Lecturer of Photogrammetry and Remote Sensing with the School of Remote Sensing and Information Engineering, Wuhan University, Wuhan. His research interests include industrial and aerial photogrammetry, 3-D reconstruction of cultural relics and buildings, automatic orthoimagery mosaicking, true orthophoto production, and parallel computing.

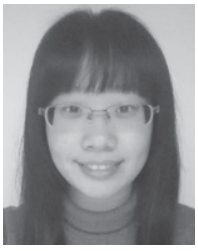

Xinyu Zhu was born in 1990. She received the B.S. degree from Wuhan University, Wuhan, China, in 2013, where she is currently pursuing the M.S. degree with the School of Remote Sensing and Information Engineering.

Her research interests include satellite remote sensing and image interpretation.